



## Directly deposited antimony on a copper silicide nanowire array as a high-performance potassium-ion battery anode with a long cycle life

Sumair Imtiaz, Nilotpai Kapuria, Ibrahim Saana Aminu, Abinaya Sankaran, SHALINI SINGH, HUGH GEANEY, TADHG KENNEDY, KEVIN M. RYAN

### Publication date

10-11-2022

### Published in

Advanced Functional Materials, 33, 2209566

### Licence

This work is made available under the [CC BY-NC-SA 4.0](#) licence and should only be used in accordance with that licence. For more information on the specific terms, consult the repository record for this item.

### Document Version

1

### Citation for this work (HarvardUL)

Imtiaz, S., Kapuria, N., Aminu, I.S., Sankaran, A., SINGH, S., GEANEY, H., KENNEDY, T. and RYAN, K.M. (2022) 'Directly deposited antimony on a copper silicide nanowire array as a high-performance potassium-ion battery anode with a long cycle life', available: <https://doi.org/10.34961/researchrepository-ul.22691965.v1>.

This work was downloaded from the University of Limerick research repository.

For more information on this work, the University of Limerick research repository or to report an issue, you can contact the repository administrators at [ir@ul.ie](mailto:ir@ul.ie). If you feel that this work breaches copyright, please provide details and we will remove access to the work immediately while we investigate your claim.

# Directly Deposited Antimony on a Copper Silicide Nanowire Array as a High-Performance Potassium-Ion Battery Anode with a Long Cycle Life

Sumair Imtiaz, Nilotpal Kapuria, Ibrahim Saana Amiinu, Abinaya Sankaran, Shalini Singh, Hugh Geaney, Tadhg Kennedy, and Kevin M. Ryan\*

Antimony (Sb) is a promising anode material for potassium-ion batteries (PIBs) due to its high capacity and moderate working potential. Achieving stable electrochemical performance for Sb is hindered by the enormous volume variation that occurs during cycling, causing a significant loss of the active material and disconnection from conventional current collectors (CCs). Herein, the direct growth of a highly dense copper silicide ( $\text{Cu}_{15}\text{Si}_4$ ) nanowire (NW) array from a Cu mesh substrate to form a 3D CC is reported that facilitates the direct deposition of Sb in a core-shell arrangement ( $\text{Sb}@_{\text{Cu}_{15}\text{Si}_4}$  NWs). The 3D  $\text{Cu}_{15}\text{Si}_4$  NW array provides a strong anchoring effect for Sb, while the spaces between the NWs act as a buffer zone for Sb expansion/contraction during K-cycling. The binder-free  $\text{Sb}@_{\text{Cu}_{15}\text{Si}_4}$  anode displays a stable capacity of  $250.2 \text{ mAh g}^{-1}$  at  $200 \text{ mA g}^{-1}$  for over 1250 cycles with a capacity drop of  $\approx 0.028\%$  per cycle. Ex situ electron microscopy revealed that the stable performance is due to the complete restructuring of the Sb shell into a porous interconnected network of mechanically robust ligaments. Notably, the 3D  $\text{Cu}_{15}\text{Si}_4$  NW CC is expected to be widely applicable for the development of alloying-type anodes for next-generation energy storage devices.

## 1. Introduction

Rapid transition from fossil fuels to renewable electricity generation technologies (e.g., solar and wind power sources) demands low-cost and reliable large-scale electrical energy storage systems (LEESs). Lithium-ion batteries (LIBs) are an obvious option due to their dominance in the portable electronic device and electric vehicle industries. However, the scarcity of Li resources, uneven geographical distribution, and the increasing market share of EVs cast uncertainties on the sustainability of Li for LEESs.<sup>[1]</sup> In this regard, there is an increasing interest in other resource-rich alkali-metal-based rechargeable battery technologies. Potassium-ion batteries (PIBs) have emerged as a promising candidate for LEESs because of the high natural abundance of K (1.5 wt% in earth's crust) and potential price advantage of potassium compounds.<sup>[2]</sup> In addition,


PIBs exhibit high energy density arising from the low standard reduction potential of  $\text{K}^+/\text{K}$  ( $-2.93 \text{ V}$  vs standard hydrogen electrode) which is very close to that of  $\text{Li}^+/\text{Li}$  ( $-3.04 \text{ V}$ ) and have a similar “rocking-chair” working principle.<sup>[2c,3]</sup> However, the large ionic radius of  $\text{K}^+$  (0.138 nm) induces slow kinetics and huge volume expansion during potassiation/de-potassiation, leading to poor cycling stability and rapid capacity decay.<sup>[4]</sup> Therefore, identifying favorable anode materials and architectures that can accommodate the large volume variation during K-cycling, while maintaining a stable and high capacity is a challenge.

Alloying-type anode materials (Sb, Bi, Sn, etc.) have received increased research attention due to their low working potential, cost-effectiveness, and high theoretical capacities.<sup>[3,5]</sup> Sb is a particularly appealing candidate for PIBs, owing to its high electrical conductivity ( $2.56 \times 10^6 \text{ S m}^{-1}$ ), safe operating voltage, and high theoretical capacity ( $\text{K}_3\text{Sb}$ ,  $660 \text{ mAh g}^{-1}$ ).<sup>[6]</sup> However, the large volume expansion ( $\approx 407\%$ ) during the K-alloying reaction causes structural instability, which remains a major obstacle to the application of Sb anodes in PIBs.<sup>[7]</sup> This challenge requires advanced structural engineering on the design of Sb-based anodes such that they can both accommodate the large volume changes during the alloying reaction and enable fast

S. Imtiaz, N. Kapuria, I. S. Amiinu, A. Sankaran, S. Singh, H. Geaney, T. Kennedy, K. M. Ryan  
Bernal Institute  
University of Limerick  
Limerick V94 T9PX, Ireland  
E-mail: kevin.m.ryan@ul.ie

S. Imtiaz, N. Kapuria, I. S. Amiinu, A. Sankaran, H. Geaney, T. Kennedy, K. M. Ryan  
Department of Chemical Sciences  
University of Limerick  
Limerick V94 T9PX, Ireland

S. Imtiaz, K. M. Ryan  
MaREI, the SFI Research Centre for Energy  
Climate and Marine  
University of Limerick  
Limerick V94 T9PX, Ireland

 The ORCID identification number(s) for the author(s) of this article can be found under <https://doi.org/10.1002/adfm.202209566>.

© 2022 The Authors. Advanced Functional Materials published by Wiley-VCH GmbH. This is an open access article under the terms of the Creative Commons Attribution License, which permits use, distribution and reproduction in any medium, provided the original work is properly cited.

DOI: 10.1002/adfm.202209566

K<sup>+</sup> diffusion kinetics. The use of Sb/carbon nanocomposites is a common strategy to improve the electrochemical performance of Sb.<sup>[8]</sup> Although this strategy has shown improvement in cycling performance, their complicated fabrication routes are disadvantageous, and the added low-capacity carbonaceous materials in the composite anodes negate the high capacity of Sb. In addition, these anodes are typically slurry processed and coated on traditional planar CCs using inactive binders, which decreases the overall energy density of the cell.<sup>[9]</sup> A 3D CC is an effective approach for constructing alloying anodes as it can provide the robust adhesion between active material and CC at a nanoscale, and allows for the direct deposition of active materials, leading to a controllably designed, self-supported, and binder-free anode. Various high surface area 3D CC architectures such as Cu nanorod array, 3D NW arrayed Cu, Ni NW array and Ni 3D bicontinuous scaffolds<sup>[10]</sup> have been employed in Li- and Na-ion batteries to anchor alloying anode materials. However, this area has received limited research attention in PIBs.

Here, we have utilized a highly dense 3D Cu<sub>15</sub>Si<sub>4</sub> NW array for the direct thermal deposition of Sb to fabricate a core-shell Sb@Cu<sub>15</sub>Si<sub>4</sub> NW array anode. The high-density Cu<sub>15</sub>Si<sub>4</sub> NW array is directly grown from a Cu mesh substrate with a woven net structure in a high boiling solvent system. The 3D Cu<sub>15</sub>Si<sub>4</sub> NW array architecture acts as a robust conductive scaffold for the direct deposition of Sb, while also providing a large surface area for Sb deposition. The 3D Cu<sub>15</sub>Si<sub>4</sub> NW array also enhances the interfacial surface area for Sb alloying with the spaces between the NWs acting as a buffer for Sb during cycling. The as-prepared Sb@Cu<sub>15</sub>Si<sub>4</sub> NW anode exhibits good cycling stability for over 1250 cycles at 200 mA g<sup>-1</sup>, with a capacity drop of only 0.028% per cycle. It further exhibits a high rate capability with the reversible capacity of 228.4 mAh g<sup>-1</sup> even at 2000 mA g<sup>-1</sup>. The effect of repeated cycling on the Sb@Cu<sub>15</sub>Si<sub>4</sub> NW array anode is investigated by ex situ high-resolution scanning and transmission electron microscopy, which show that the Cu<sub>15</sub>Si<sub>4</sub> NWs remain intact and mechanically stable, enabling the Sb coating to transform into a highly porous interconnected network of ligaments that remains well adhered to the CC.

## 2. Results and Discussion

The synthesis of the binder-free Sb@Cu<sub>15</sub>Si<sub>4</sub> NW array anode is schematically presented in **Figure 1a**. The pristine Cu mesh has a woven net structure comprising of a smooth surface with a mesh opening of ≈55–57 μm and a wire diameter of ≈40 μm (**Figure 1b**). The Cu<sub>15</sub>Si<sub>4</sub> NWs were grown in situ by the decomposition of phenylsilane, directly on the Cu mesh architecture in a solvent vapor growth system.<sup>[11a,13]</sup> The low and high-magnification SEM images (**Figure 1c,d**) of the as-grown Cu<sub>15</sub>Si<sub>4</sub> NWs show uniform coverage and high density of NWs on the Cu mesh CC, with the average diameter of ≈99 nm (inset **Figure 1d**) and are in micrometer lengths. SEM images of the cross-section (**Figure 1e–g**) further reveal that the Cu<sub>15</sub>Si<sub>4</sub> NWs interfaced directly through the parent Cu mesh. In addition, the well-ordered woven net structure of the Cu mesh CC remained fully intact after the high boiling solvent VSS reaction (**Figure 1c**). **Figure 1h** shows the TEM image of a single Cu<sub>15</sub>Si<sub>4</sub>

NW. The high-resolution TEM (HRTEM) image and corresponding fast Fourier transform (FFT) diffractogram of the Cu<sub>15</sub>Si<sub>4</sub> NW shown in **Figure 1i,j** reveals the crystalline structure with the *d*-spacing of 0.34 nm, in agreement with previous reports on Cu<sub>15</sub>Si<sub>4</sub>.<sup>[11]</sup>

The Sb coating on the Cu<sub>15</sub>Si<sub>4</sub> NW array CC was deposited using a vacuum-based thermal evaporator. The low and high-magnification images (**Figure 2a–c**, and **Figure S1a–c**, Supporting Information) show that the as-deposited Sb@Cu<sub>15</sub>Si<sub>4</sub> NW array CC replicates the morphology of the 3D Cu<sub>15</sub>Si<sub>4</sub> NW array. The well-maintained 3D open architecture of the Sb@Cu<sub>15</sub>Si<sub>4</sub> NW array is highly advantageous for enhancing electrolyte penetration over the entire anode. The coated Sb@Cu<sub>15</sub>Si<sub>4</sub> NWs diameter increased to an average of ≈180 nm (**Figure S1d**, Supporting Information). **Figure 2d** shows the low and high-magnification TEM images of Sb@Cu<sub>15</sub>Si<sub>4</sub> NW, which clearly indicate a fully coated Cu<sub>15</sub>Si<sub>4</sub> NW with Sb and slightly rougher surface morphology compared to the pristine Cu<sub>15</sub>Si<sub>4</sub> NW (**Figure 1h**). The HRTEM image (**Figure 2e**) confirmed the crystalline nature of the Sb layer with a lattice spacing of 0.31 nm, corresponding to the (012) planes of metallic Sb.<sup>[14]</sup> The XRD pattern of the Sb@Cu<sub>15</sub>Si<sub>4</sub> NW array (**Figure S2**, Supporting Information) also reveals the presence of crystalline Sb (JCPDS Card No.: 00-001-0802), along with Cu, Cu<sub>15</sub>Si<sub>4</sub>, and Cu<sub>0.83</sub>Si<sub>0.17</sub> in agreement with the previous reports.<sup>[10b,11a,13,15]</sup> The additional reflections of Cu<sub>0.83</sub>Si<sub>0.17</sub> in XRD and absence of this phase in the TEM analysis of nanowire suggest that it only exists in a preformed silicide layer on the Cu foil surface prior to the Cu<sub>15</sub>Si<sub>4</sub> nanowire growth,<sup>[11a,16]</sup> and that is the reason it was not identified the HRTEM analysis of NWs (**Figure 1j**). The Raman spectrum of the Sb@Cu<sub>15</sub>Si<sub>4</sub> NW array shown in **Figure S3** (Supporting Information) displays two peaks at 146.3 and 110 cm<sup>-1</sup> which are attributed to the A<sub>1g</sub> and E<sub>g</sub> bands of Sb, respectively.<sup>[8d,17]</sup> The Dark-field scanning transmission electron microscopy (DF-STEM) micrograph did not show a clear contrast between the Sb shell and Cu<sub>15</sub>Si<sub>4</sub> NW core. However, the energy dispersive X-ray (EDX) elemental mapping of Sb@Cu<sub>15</sub>Si<sub>4</sub> NW confirmed the presence of a Cu<sub>15</sub>Si<sub>4</sub> NW core, completely encapsulated by the Sb shell (**Figure 2f**). Furthermore, the digital photographs show a visual change of the substrate color from a characteristic red-orange metallic luster to a gray/brown after Cu<sub>15</sub>Si<sub>4</sub> NWs synthesis and then to silvery metallic after depositing Sb (**Figure S4**, Supporting Information).

The electrochemical performance of Sb@Cu<sub>15</sub>Si<sub>4</sub> NW array as a K-ion anode was assessed in a half-cell configuration in a CR2032 coin cell and compared with Sb@Cu mesh (Sb film directly evaporated onto the Cu mesh) as a control. Cyclic voltammetry (CV) profiles of the Sb@Cu<sub>15</sub>Si<sub>4</sub> NW array in **Figure 3a** shows the initial ten CV curves at the scan rate of 0.1 mV s<sup>-1</sup> in the voltage range of 0.01–1.5 V. The first cathodic CV scan is clearly different from the latter scans, where a broad peak at ≈900 mV is observed, predominantly due to electrolyte decomposition and solid electrolyte interphase (SEI) layer formation.<sup>[18]</sup> In the following cycles, the cathodic peaks at ≈570 mV and below 200 mV can be assigned to the formation of K<sub>x</sub>Sb and K<sub>3</sub>Sb phases, respectively. During the anodic scans, two peaks are displayed at ≈390 and 700 mV, which can be attributed to the de-potassiation reactions of K<sub>3</sub>Sb and the formation of Sb, respectively.<sup>[14,18b,19]</sup> The cathodic and anodic

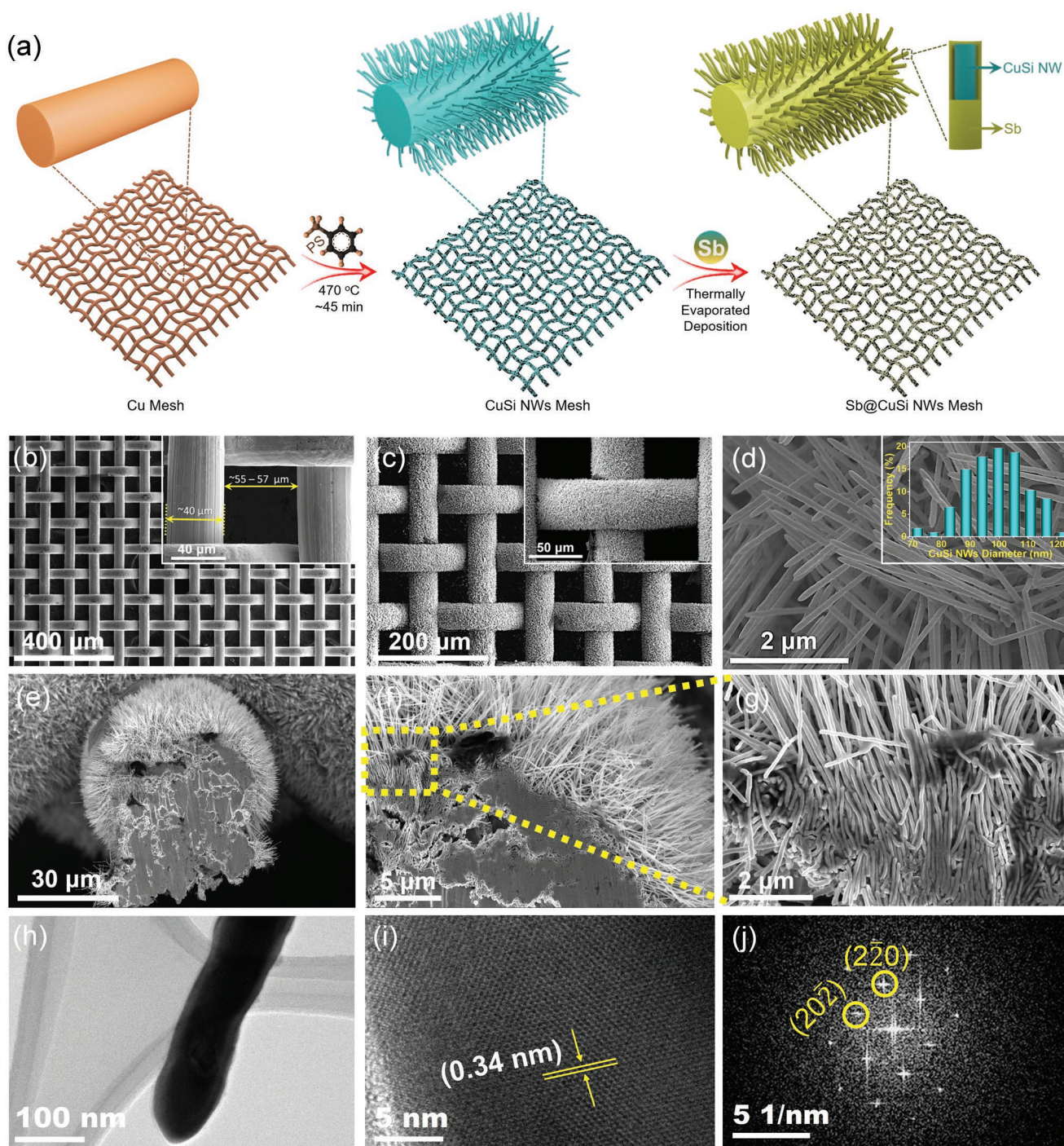


**Figure 1.** a) Schematic illustration of the synthesis of the  $\text{Cu}_{15}\text{Si}_4$  NW array current collector and thermally evaporated deposition of Sb, corresponding magnified schematic showing plain Cu mesh fiber,  $\text{Cu}_{15}\text{Si}_4$  NW growth fiber, and  $\text{Sb}@_{\text{Cu}_{15}\text{Si}_4}$  NWs fiber; b) low magnification SEM image of pristine Cu mesh, inset showing the mesh opening and wire diameter of mesh; c) low and inset higher magnification SEM images of the as-grown dense  $\text{Cu}_{15}\text{Si}_4$  NWs on Cu mesh CC; d) high magnification SEM images of the as-grown dense  $\text{Cu}_{15}\text{Si}_4$  NWs on Cu mesh CC, an inset in Fig. d representing average  $\text{Cu}_{15}\text{Si}_4$  NW diameter distribution; Cross-sectional SEM images e) low, f,g) higher-magnification of the  $\text{Cu}_{15}\text{Si}_4$  NW array substrate representing the tree-root like growth features; h) TEM image of a single  $\text{Cu}_{15}\text{Si}_4$  NW and i) HRTEM image, and j) selected area FFT diffraction pattern showing the crystallinity of the  $\text{Cu}_{15}\text{Si}_4$  NW.

peaks display consistent positions and tend to overlap, demonstrating the high reversibility and stabilization of the potassium/de-potassium processes.<sup>[18c,20]</sup> Figure 3b shows the

voltage profiles of the  $\text{Sb}@_{\text{Cu}_{15}\text{Si}_4}$  NW array for selected cycles, which represents the typical charge/discharge profiles of Sb in PIBs and is consistent with previous studies.<sup>[8a,18b,21]</sup> The

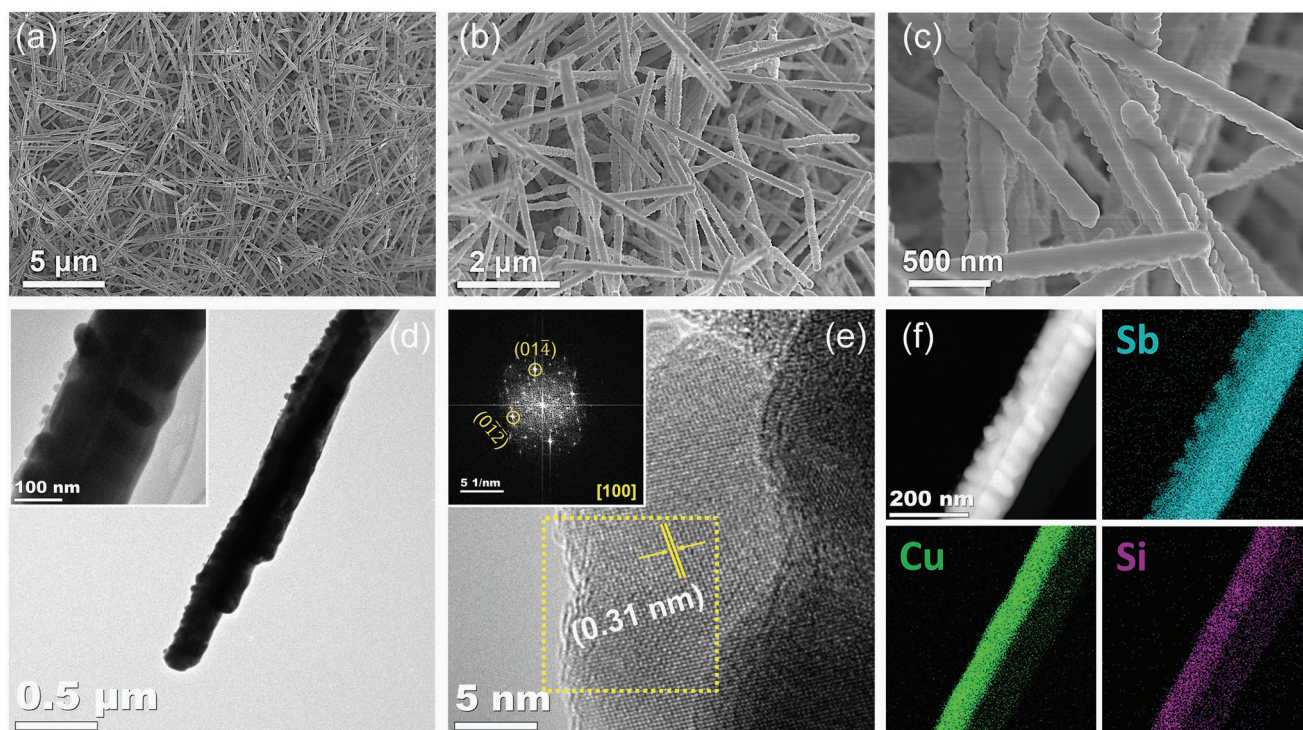


**Figure 2.** a–c) SEM images of the Sb@Cu<sub>15</sub>Si<sub>4</sub> NW array anodes at different magnifications, d) representative TEM images of Sb@Cu<sub>15</sub>Si<sub>4</sub> NWs, e) HRTEM image, and inset is the selected area FFT diffraction pattern of as-deposited Sb, and f) DFSTEM image of the Sb@Cu<sub>15</sub>Si<sub>4</sub> NW with corresponding EDX elemental maps for Sb (aqua blue), Cu (green) and Si (purple).

differential capacity plots (DCP) extracted from the voltage profiles show a similar trend to the CV scan (Figure 3c). Comparison of the DCP of the 2<sup>nd</sup> cycle of Sb@Cu<sub>15</sub>Si<sub>4</sub> NWs and Sb@Cu mesh anode shows an interesting difference, where an additional peak at ≈900 mV associated with the formation of the SEI layer is observed for Sb@Cu<sub>15</sub>Si<sub>4</sub> NWs (Figure 3c),<sup>[22]</sup> whereas, the DCP of the 2<sup>nd</sup> cycle for Sb@Cu mesh did not show a similar peak (Figure S5, Supporting Information). This further indicates that additional electrolyte decomposition occurs in the case of the Sb@Cu<sub>15</sub>Si<sub>4</sub> NW array due to the enhanced penetration of electrolyte, providing higher availability of Sb for alloying/de-alloying. This peak disappears for the following cycles and the DCP remains consistent beyond this, indicating excellent stability of the Sb@Cu<sub>15</sub>Si<sub>4</sub> NW array anode. Figure 3d compares the long-term cyclability performance of the Sb@Cu<sub>15</sub>Si<sub>4</sub> NW array with that of Sb@Cu mesh. The current density of the initial five cycles was set at 50 mA g<sup>-1</sup> and the following cycles were as 200 mA g<sup>-1</sup>. The Sb@Cu<sub>15</sub>Si<sub>4</sub> NW array displays a high initial reversible capacity of 647.9 mAh g<sup>-1</sup> at 50 mA g<sup>-1</sup>, representing 98.2% of the theoretical capacity of Sb (660 mAh g<sup>-1</sup>). The capacity dropped to 556.8 mAh g<sup>-1</sup> after five cycles. After initial activation at 50 mA g<sup>-1</sup>, the current density was increased to 200 mA g<sup>-1</sup>, and Sb@Cu<sub>15</sub>Si<sub>4</sub> NW array shows a capacity of 386.2 mAh g<sup>-1</sup> and maintaining outstanding cycling stability, delivering a capacity of 250.2 mAh g<sup>-1</sup> even after 1250 cycles. This represents a capacity retention of ≈65% (Figure S6, Supporting Information) and a capacity drop of only 0.028% per cycle (calculated from the 6<sup>th</sup> cycle onwards, where the applied current density was raised to 200 mA g<sup>-1</sup>)

with an average Coulombic efficiency of 98.3%. On the other hand, the Sb@Cu mesh showed a continuous drop in capacity, retaining <100 mAh g<sup>-1</sup> after only 200 cycles. It is worth noting that the Cu<sub>15</sub>Si<sub>4</sub> NW array alone did not show any contribution to the capacity and remained inactive during charge/discharge as illustrated in Figure S7 (Supporting Information). The excellent cycling stability of the Sb@Cu<sub>15</sub>Si<sub>4</sub> NW array compared to the Sb@Cu mesh attests to the robust electrical contact of Sb with Cu<sub>15</sub>Si<sub>4</sub> NWs, high surface area, and excellent anchoring effect provided by the NWs.

The rate capability performance of the Sb@Cu<sub>15</sub>Si<sub>4</sub> NW array anode was analyzed and compared with Sb@Cu mesh at various rates by charging and discharging for five cycles at 50, 100, 200, 400, 600, 800, 1000, 1500, 2000, 2500, 3000, 3500, 4000, and back to 50 mA g<sup>-1</sup> (Figure 3e). The Sb@Cu<sub>15</sub>Si<sub>4</sub> NW array exhibit much better rate performance at the various current densities than the Sb@Cu mesh. The Sb@Cu<sub>15</sub>Si<sub>4</sub> NW array electrode maintains a high reversible capacity of 228.4 mAh g<sup>-1</sup> at 2000 mA g<sup>-1</sup>, whereas, the Sb@Cu mesh electrode shows negligible capacities at 2000 mA g<sup>-1</sup> and above. The galvanostatic charge/discharge profiles of the Sb@Cu<sub>15</sub>Si<sub>4</sub> NW electrode at various current densities are presented in Figure 3f. Upon close examination, it can be seen that the shape of voltage profiles at current densities higher than 2000 mA g<sup>-1</sup> is different. The DCPs (Figure S8, Supporting Information) extracted from these voltage profiles show that the potassiation peak at ≈260 mV at 50 mA g<sup>-1</sup> continues to shift towards the lower potentials with an increase in current density, reaching ≈150 mV at 2000 mA g<sup>-1</sup> and then diminishes in magnitude

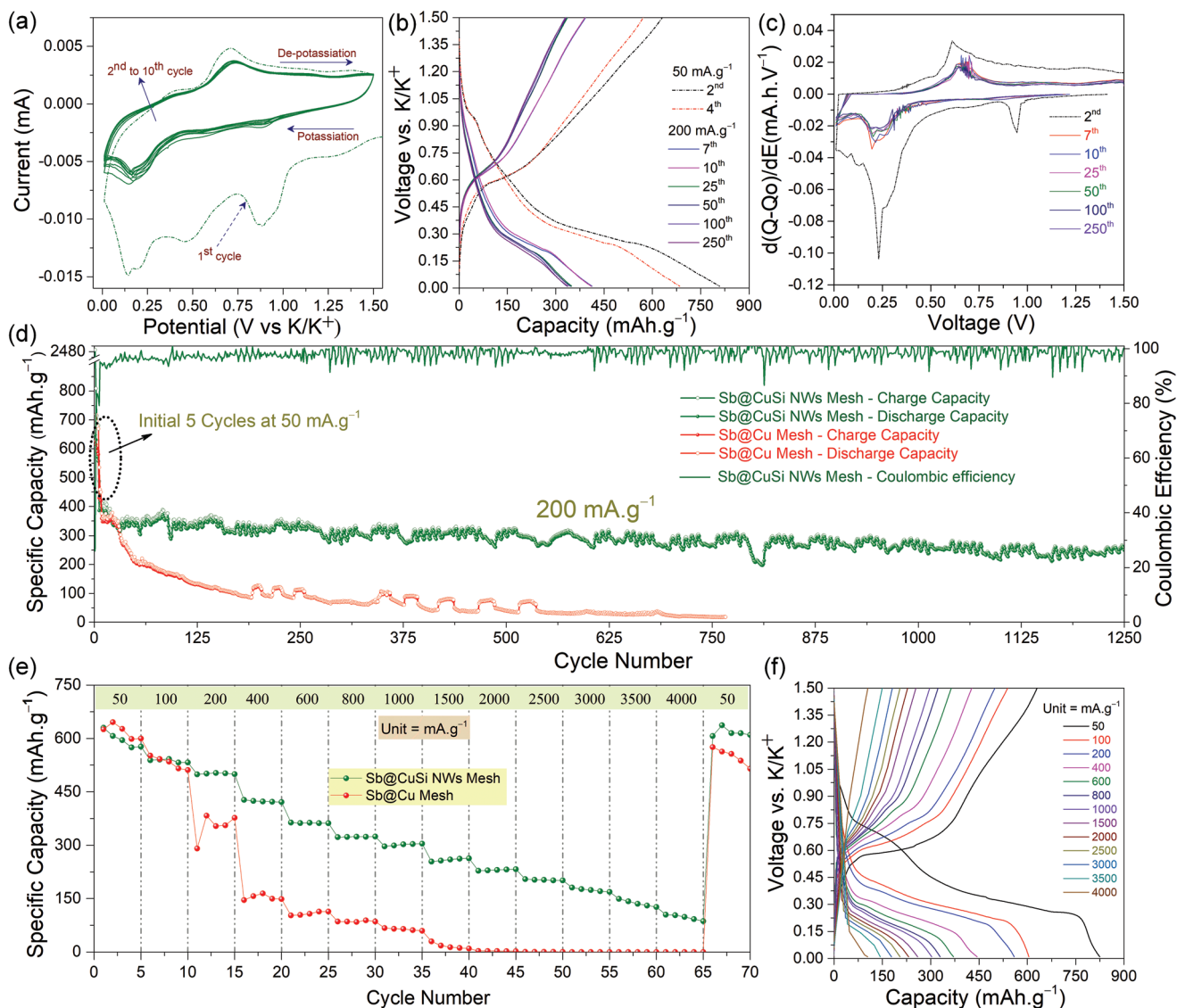


**Figure 3.** Electrochemical performance of the Sb@Cu<sub>15</sub>Si<sub>4</sub> NW array anode. a) CV profiles of Sb@Cu<sub>15</sub>Si<sub>4</sub> NW array, b) Galvanostatic charge/discharge voltage profiles of Sb@Cu<sub>15</sub>Si<sub>4</sub> NW array anode at 50 mA g<sup>-1</sup> (2nd and 4th) and 200 mA g<sup>-1</sup> (7th, 10th, 25th, 50th, 100th and 250th cycle), c) Differential capacity plots of 2nd, 7th, 10th, 25th, 50th, 100th and 250th cycle, d) Long-term cycling stability of Sb@Cu<sub>15</sub>Si<sub>4</sub> NW array and Sb@Cu mesh samples, e) Rate capability of Sb@Cu<sub>15</sub>Si<sub>4</sub> NW array and Sb@Cu mesh samples at various current densities, and f) Galvanostatic charge–discharge voltage profiles of Sb@Cu<sub>15</sub>Si<sub>4</sub> NW array anode at different current densities from 50 to 4000 mA g<sup>-1</sup>.

beyond that. It is observed that beyond the current density of 2000 mA g<sup>-1</sup>, the two peaks for the potassiation/de-potassiation process become a single peak. This indicates that the overpotential increases at higher current densities, which shifts the reaction potentials due to electrochemical polarization. Thus, the capacity at higher current densities decreases due to inhibited K<sup>+</sup> diffusion and incomplete potassiation. Nevertheless, the Sb@Cu<sub>15</sub>Si<sub>4</sub> NW array still displays capacities of 204.8, 181.3, 149.5, 104.9 mAh g<sup>-1</sup> at the higher current densities of 2500, 3000, 3500, 4000 mA g<sup>-1</sup>, respectively. Moreover, the reversible capacity recovered to 606.95 mAh g<sup>-1</sup> (96.3% of the initial values), when the current density reverted from 4000 to 50 mA g<sup>-1</sup>, indicating excellent stability of the nanostructured active material despite the huge stresses from the higher current densities.

The potassiation/de-potassiation mechanism of the Sb@Cu<sub>15</sub>Si<sub>4</sub> NW array was also evaluated by ex situ XRD and Raman analysis (Figure S9, Supporting Information). Notably, no XRD signals related to Sb were detected after full potassiation (0.01 V) and de-potassiation (1.5 V) possibly due to the reduced crystallinity (amorphization) of the final products.<sup>[23]</sup> However, a broad peak located at ≈140 cm<sup>-1</sup> was detected after full potassiation in Raman analysis, which is indexed to the cubic K<sub>3</sub>Sb phase. Upon de-potassiation, the emergence of Raman modes for Sb was obviously clear. The characteristic Raman peak for Sb located at 146.3 cm<sup>-1</sup> recover but its intensity is reduced. While the peak at 110 cm<sup>-1</sup> also reduces in intensity and shifts to the higher side, indicating the formation of amorphous Sb, in agreement with the previous reports.<sup>[8a,17,19b,23,24]</sup>

The Sb@Cu<sub>15</sub>Si<sub>4</sub> NW array cycling data show that the capacity losses beyond 100 cycles are minimal ( $\approx 0.017\%$  per cycle), which indicates that Sb has transformed into a stable structure. To examine this, we evaluated the structural changes occurring at the anode after 1, 10, 25, 50, and 100 cycles by an ex situ electron microscopic study. The ex situ SEM image of the anode after the first potassiation shows intense morphological changes of Sb due to the alloying with K<sup>+</sup>, causing a volume expansion (Figure S10, Supporting Information). The

ex situ SEM and TEM images of the anode after 1 cycle (in the de-potassiated state) show a textured Sb shell that is obviously different in morphology (Figure 4a,b) compared to the pristine anode (Figure 2c). The formation of a textured morphology of the Sb shell is due to the extraction sites of K during de-potassiation process that produces vacancies. This phenomenon has been previously discovered for Li-alloying (Si, Ge, Sn) anode materials.<sup>[13,25]</sup> The texturing of the Sb layer has become more significant after ten cycles (Figure 4d) with the presence of

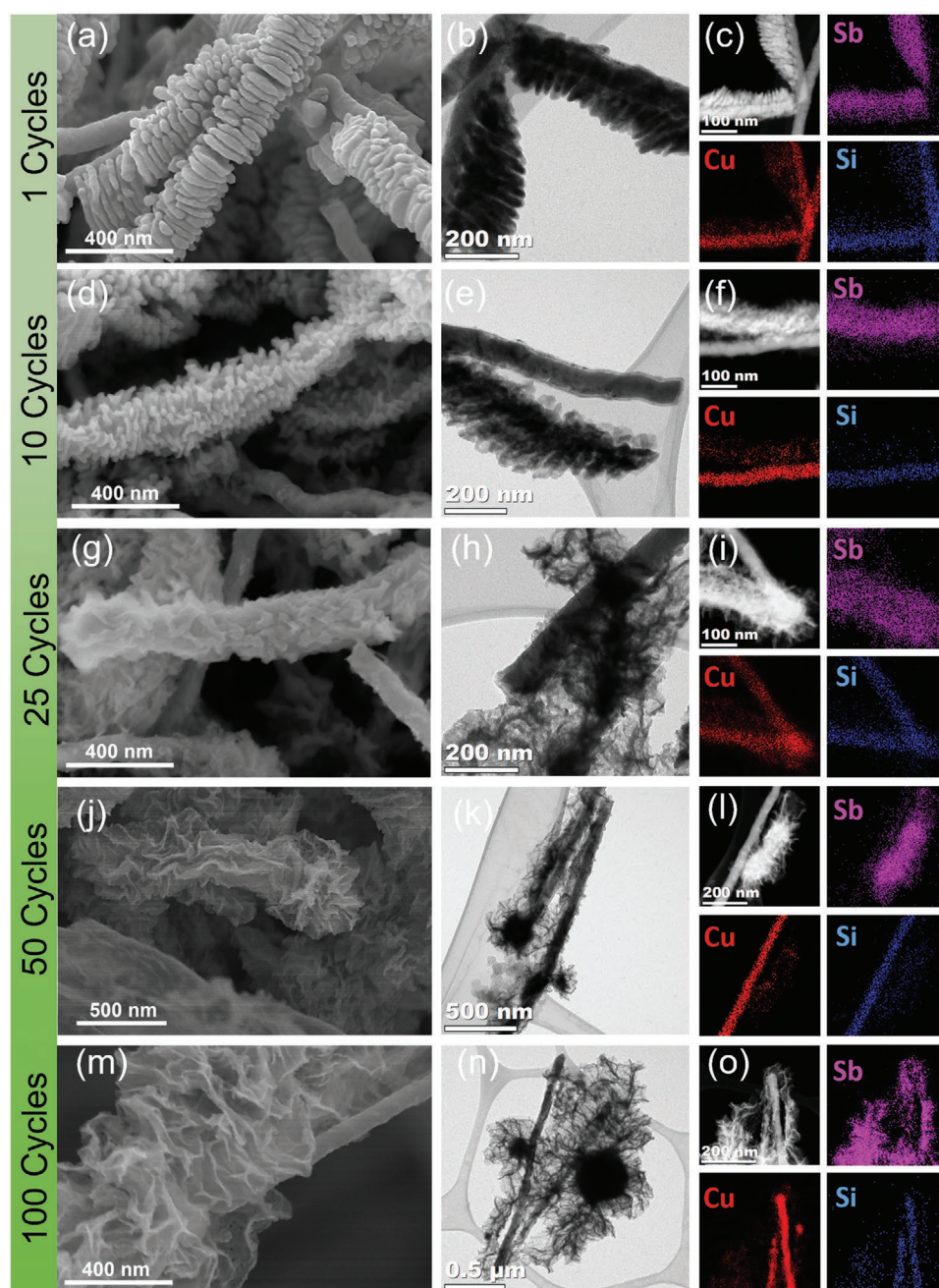


**Figure 4.** Ex situ SEM, TEM, and DFSTEM image of the Sb@Cu<sub>15</sub>Si<sub>4</sub> NW array with corresponding EDX elemental maps for Sb (magenta), Cu (red), and Si (blue) after a–c) 1 Cycle, d–f) 10 cycles, g–i) 25 cycles j–l) 50 cycles, and m–o) 100 cycles, respectively. The complete restructuring of the Sb to the mechanically robust porous interconnected network Sb ligaments is apparent, whereas the Cu<sub>15</sub>Si<sub>4</sub> NWs remain intact without any visible fracture and fragmentation, indicating mechanical stability.

grooves and ridges, due to the agglomeration of more K extraction sites. The TEM image (Figure 4e) confirms the noticeably enriched texturing of the Sb shell after 10 cycles. The deformation of the Sb shell is more intense after 25 cycles (Figure 4g), and the TEM image indicates that surface textures have started to form a system of Sb ligaments (Figure 4h). After 50 cycles (Figure 4j,k) the morphology of the seemingly fused-particulate feature of the Sb shell has completely transformed into an interconnected porous network of ligaments due to the agglomeration and fusion of neighboring active material. The ex situ SEM and TEM of the Sb@Cu<sub>15</sub>Si<sub>4</sub> NWs after 100 cycles further demonstrate the evidence of fusion and agglomeration between neighboring nanostructured Sb, confirming the complete restructuring of the material into the porous ligament morphology (Figure 4m,n). The detailed investigation of this as-formed network after 100 cycles was analyzed by HRTEM (Figure S11a, Supporting Information), which shows that it is comprised of a porous interconnected structure of interwoven Sb ligaments, whereby the mean ligament diameter is ≈7.9 nm (Figure S11b, Supporting Information). The formation of this porous network is highly advantageous as the ligament's structure is mechanically robust and highly stable and once formed, it exhibits no further significant deformation thereafter, leading to a long cycle life.<sup>[20a,25a,26]</sup> The abundant spaces within the network of porous ligaments can provide extra space to cushion the volume variation during cycling.<sup>[20a,27]</sup> The stability of this interconnected porous Sb ligament structure is also evident from the long-term cycling performance results (Figure 3d) where the capacity remains stable after 100 cycles.

The DFSTEM images and corresponding elemental mapping tracks the signals of Sb, Cu, and Si after 1, 10, 25, 50, and 100 cycles (Figure 4c,f,i,l,o) and show that the Cu<sub>15</sub>Si<sub>4</sub> NWs remain localized without any deformation or fracture. This is significant as in the case of LIBs, the Cu<sub>15</sub>Si<sub>4</sub> NWs were found to be fractured due to anisotropic expansion-induced strain.<sup>[13]</sup> However, no evidence of fracture or fragmentation of the Cu<sub>15</sub>Si<sub>4</sub> NWs is detected here, which shows the high durability and compatibility of this host architecture as a CC for PIBs. The low and high magnification SEM images of the Sb@Cu<sub>15</sub>Si<sub>4</sub> NW array anode after 100 cycles show that the active material remains well adhered to the Cu<sub>15</sub>Si<sub>4</sub> NW array CC (Figure S12, Supporting Information). While a few bare Cu<sub>15</sub>Si<sub>4</sub> NWs can be seen at some instances, on the whole, the active material remained in good contact with Cu<sub>15</sub>Si<sub>4</sub> NWs due to the formation of interconnected structure Sb ligaments. In contrast, the Sb@Cu mesh showed extensive active material delamination (Figures S13, and S14, Supporting Information). This Sb@Cu mesh also shows the transformation of morphology towards a textured surface. However, the formation of porous ligaments cannot be seen, this shows that the formation of porous Sb ligaments is enabled by the strong anchoring effect provided by the Cu<sub>15</sub>Si<sub>4</sub> NWs and the availability of buffer zone to allow Sb to expand freely during potassiation/de-potassiation. As can be seen from the SEM image after 100 cycles (Figure 4m), the Sb shell expanded to ≈746 nm. Considering the mean diameter of pristine Sb shell ≈188 nm (Figure S1d, Supporting information), this corresponds to a total volume expansion of ≈425% (including the pore spaces).

GITT is used to obtain the K<sup>+</sup> diffusion coefficient during first potassiation and de-potassiation, which can intuitively reflect the diffusion kinetics of K<sup>+</sup> in the Sb@Cu<sub>15</sub>Si<sub>4</sub> NW array. The diffusion coefficient of K<sup>+</sup> in the electrode is calculated based on Fick's second law of diffusion as follows:<sup>[28]</sup>

$$D_k = \frac{4}{\pi\tau} \left( \frac{m_B V_m}{M_b S} \right)^2 \left( \frac{\Delta E_s}{\Delta E_r} \right)^2 \quad (1)$$

where  $\tau$  is the time of applying a Galvanostatic pulse;  $m_B$  is the active mass in the anode;  $V_m$  and  $M_b$  are the molar volume and molar mass of the active material, respectively;  $S$  represents the geometry area of the electrode; and  $\Delta E_s$  and  $\Delta E_r$  are obtained from GITT curve as explained in Figure S15 (Supporting Information). Figure S16 (Supporting Information) presents the GITT curve obtained from the Sb@Cu<sub>15</sub>Si<sub>4</sub> NW array and the calculated K<sup>+</sup> diffusion coefficient ( $D_k$ ). It can be observed that  $D_k$  during the de-potassiation process is substantially higher than that of the potassiation process, which indicates that de-potassiation is facile to carry out than the potassiation process.<sup>[29]</sup> This further compliments the morphological changes observed by ex situ SEM during the first cycle (Figure S10, Supporting Information, and Figure 4a). An intense morphological change of Sb occurs after the first potassiation, providing enhanced channels for K<sup>+</sup> diffusion during de-potassiation, as a result, the diffusion of K<sup>+</sup> in the de-potassiation process is easier. EIS was used to further gain insight into the electrochemical performance. The EIS spectra of Sb@Cu<sub>15</sub>Si<sub>4</sub> NW array and Sb@Cu mesh electrode after 1st and 50th cycles are presented in Figure S17 (Supporting Information). The equivalent circuit used in the analysis is shown in the inset of Figure S17a (Supporting information), where  $R_s$  is the electrolyte resistance,  $R_{sei}$  denotes the resistance to K-ion migration through the SEI layer, and the  $R_{ct}$  is the charge transfer resistance. The  $Q_{sei}$  and  $Q_{dl}$  are the constant phase elements corresponding to the capacitances of the SEI layer and electrochemical double layer, and  $W$  is Warburg impedance related to K-ion diffusion.<sup>[30]</sup> The values obtained are listed in Table S1 (Supporting Information). After the 1st cycle, the  $R_{sei}$  and  $R_{ct}$  values obtained for both Sb@Cu<sub>15</sub>Si<sub>4</sub> NW array and Sb@Cu mesh anode are comparable. The high initial  $R_{sei}$  value for the Sb@Cu<sub>15</sub>Si<sub>4</sub> NW array anode is also apparent from the CV (Figure 3a), due to the large area available in contact with the electrolyte. Interestingly, a huge difference in  $R_{sei}$  and  $R_{ct}$  of Sb@Cu<sub>15</sub>Si<sub>4</sub> NW array and Sb@Cu mesh anode is observed after 50 cycles, which significantly decreased for the Sb@Cu<sub>15</sub>Si<sub>4</sub> NW array anode. This significant decrease in resistance after 50 cycles indicates good active material contact with the Cu<sub>15</sub>Si<sub>4</sub> NWs, and stable SEI formation during cycling; as a result, improved capacity retention and rate capability are obtained. In addition, in Sb@Cu mesh electrode, the slope of the oblique line which is related to K<sup>+</sup> diffusion becomes smaller after 50 cycles, suggesting that the K<sup>+</sup> diffusion becomes difficult with cycling. While, the slope line region of 3D Sb@Cu<sub>15</sub>Si<sub>4</sub> NW array electrode is much more pronounced after 50 cycles, which demonstrates that the K<sup>+</sup> diffusion is improved with cycling. This could be due to the transformation of Sb into a stable porous ligament network structure, which offers a larger surface area that can accommodate more facile charge transfer during electrochemical



cycling.<sup>[31]</sup> Importantly, it should be noted that a large portion of the Cu mesh is still retained as a part of the anode (Sb@Cu<sub>15</sub>Si<sub>4</sub> NW array) even after the growth of Cu<sub>15</sub>Si<sub>4</sub> NWs and given that Cu-silicide is an intermetallic with excellent conductivity properties,<sup>[13,15]</sup> a high proportion of overall conductivity is reserved by the Cu<sub>15</sub>Si<sub>4</sub> NW array substrate.

Overall, the superior K-storage capability and cyclability of the Sb@Cu<sub>15</sub>Si<sub>4</sub> NW array architecture can be ascribed to the 3D structure of the Cu<sub>15</sub>Si<sub>4</sub> NW framework, which allows direct deposition of high-capacity Sb. The schematic in **Figure 5a,b** depicts the enhanced K-storage mechanism of the Sb@Cu<sub>15</sub>Si<sub>4</sub> NW array, where the structural design can enhance electrolyte penetration, providing high contact area and a strong anchoring effect. Furthermore, this architecture can facilitate the rapid transport of K<sup>+</sup>, and the spaces between NWs can buffer the huge volumetric change of Sb during potassiation/de-potassiation. Thus, the synergistic effect of the permeable 3D structure of the self-supported and binder-free Sb@Cu<sub>15</sub>Si<sub>4</sub> NW array features allows a significant boost in performance and stability over reported studies as presented in Table S2 (Supporting Information), validating the high promise of the Cu<sub>15</sub>Si<sub>4</sub> NW array architectures for application in high-energy-density PIBs.

### 3. Conclusion

In summary, we demonstrate the direct growth of highly dense Cu<sub>15</sub>Si<sub>4</sub> NWs from a Cu mesh substrate as a 3D CC through a simple high boiling solvent VSS growth mechanism. Elemental Sb is directly evaporated onto the Cu<sub>15</sub>Si<sub>4</sub> NW array to fabricate a core-shell Sb@Cu<sub>15</sub>Si<sub>4</sub> NW array anode. The combined effect of conductive NWs and permeable mesh structure of the as-fabricated Sb@Cu<sub>15</sub>Si<sub>4</sub> NW array anode displays a high initial reversible capacity of 647.9 mAh g<sup>-1</sup> at 50 mA g<sup>-1</sup> and exhibits good cycling stability for over 1250 cycles at 200 mA g<sup>-1</sup>. The ex situ SEM and TEM analysis of Sb@Cu<sub>15</sub>Si<sub>4</sub> NW array after cycling showed a complete restructuring of the Sb shell to the mechanically robust porous interconnected of Sb ligaments, while the Cu<sub>15</sub>Si<sub>4</sub> NWs remain mechanically stable. Furthermore, the simple and effective nature of this work highlights a feasible route to significantly address the issues related to high-capacity alloying anode materials.

### 4. Experimental Section

**Synthesis of Cu<sub>15</sub>Si<sub>4</sub> NW Array on Cu Mesh:** The synthesis of Cu<sub>15</sub>Si<sub>4</sub> NW array was carried out using a high boiling solvent-mediated vapor-solid-solid (VSS) growth mechanism with slight modifications.<sup>[11]</sup> The growth mechanism for the Cu<sub>15</sub>Si<sub>4</sub> NWs by VSS was well explained previously by Geaney et al.<sup>[11a]</sup> Briefly, Cu<sub>15</sub>Si<sub>4</sub> NWs grow directly from crystallites of the same Cu silicide film. The phenylsilane (PS) precursor decomposed in the vapor phase of a high boiling solvent that allowed the formation of copper silicide crystallite film on the solid Cu mesh by the reaction of silane vapor and Cu. The continued supply of Si vapor led to the formation of NWs from nucleation sites on the preformed crystallites, followed by a growth of dense solid Cu<sub>15</sub>Si<sub>4</sub> NW array, and was facilitated by the high diffusivity of Cu in Si.<sup>[12]</sup> In a typical reaction, a strip (≈12 × 140 mm) of copper (Cu) mesh (99.99%, 300 mesh, wire diameter: ≈40 μm, mesh opening = 55 – 57 μm) was ultrasonically washed in acetone and then thoroughly dried in air. After that, the strip of Cu mesh was attached to a custom-built stainless steel holder and placed vertically in a long-neck round-bottomed flask containing ≈7.5 mL of squalane (96.0%). The flask was then connected to a Schlenk line setup via a water condenser and positioned inside a three-zone type furnace. The temperature of the three-zone furnace was then increased up to 160 °C, and a vacuum of ≈100 × 10<sup>-3</sup> Torr was applied for 45 min to eliminate any moisture from the system. Thereafter, the system was purged with argon (Ar) gas, and the temperature raise to 470 °C under a constant flow of Ar. A water condenser was employed to control the reflux and to keep the reaction under control. After keeping the system at the desired temperature for ≈15 min., 0.8 mL of phenylsilane (PS) (97%) was injected into the system through a septum cap sealing the condenser. After 20 min of reaction, an additional 0.4 mL of PS was introduced, and the reaction continued for another 25 min. The reaction was stopped by switching off the furnace, which was subsequently allowed to cool naturally to room temperature. The obtained Cu<sub>15</sub>Si<sub>4</sub> NW-covered mesh substrates were then removed from the flask, thoroughly rinsed with toluene to remove any residual squalane, dried, and stored in the Ar-filled glovebox until further use.

**Preparation of Antimony Decorated Cu<sub>15</sub>Si<sub>4</sub> NW Array:** Antimony coatings on the Cu<sub>15</sub>Si<sub>4</sub> NW array were deposited using a vacuum-based thermal evaporator operated at 6 × 10<sup>-6</sup> bar in a glovebox-based evaporation unit. By varying the parameters such as the amount of Sb (99.999%, Kurt J. Lesker), deposition time, and deposition rate, the mass loading of the Sb layer could be tuned. Accordingly, the Sb coatings on Cu<sub>15</sub>Si<sub>4</sub> NW array were deposited leading to the mass loading of 0.075 – 0.11 mg cm<sup>-2</sup>. The sample weight was determined using a Sartorius Microbalance (Sartorius SE2, ± 0.25 μg repeatability). The as-prepared Sb@Cu<sub>15</sub>Si<sub>4</sub> NW array electrodes were stored in the Ar-filled glovebox (< 0.1 ppm O<sub>2</sub>/H<sub>2</sub>O) prior to cell assembly. As a control experiment, Sb film was directly evaporated onto the Cu mesh using similar conditions and denoted as Sb@Cu mesh.

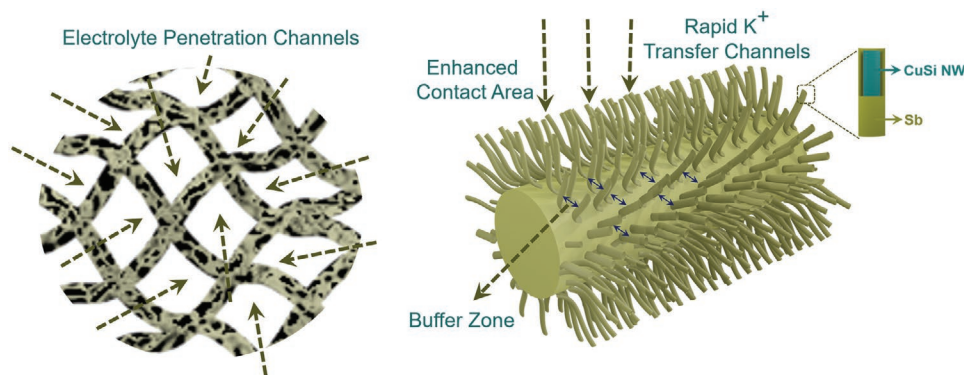


**Figure 5.** a,b) Schematic representation of enhanced k-storage mechanism of Sb@Cu<sub>15</sub>Si<sub>4</sub> NW array.

**Materials Characterization:** Scanning electron microscopy (SEM) analysis was carried out using a FEI Helios G4 CX microscope system equipped with an EDX analyzer and operated at 5–10 kV. Transmission electron microscopy (TEM) analysis was conducted on JEOL JEM-2100F field emission microscope equipped with a Gatan Ultrascan CCD camera and EDAX Genesis EDS detector and operated at 200 kV. For TEM analysis,  $\text{Cu}_{15}\text{Si}_4$  NWs and  $\text{Sb@Cu}_{15}\text{Si}_4$  NWs were removed from the substrate through ultrasonication in ethanol, and drop cast onto a lacey carbon TEM grid (200 mesh Ni). The size distribution of  $\text{Cu}_{15}\text{Si}_4$  NWs,  $\text{Sb@Cu}_{15}\text{Si}_4$  NW arrays from SEM images, and the size of ligaments in TEM image were calculated by Nano Measurer 1.2 software, and the data plotted in the form of a bar chart. X-ray diffraction (XRD) patterns were collected on PANalytical Empyrean diffractometer equipped with a PIXcel<sup>3D</sup> detector and  $\text{CuK}\alpha$  radiation source ( $\lambda = 1.5406 \text{ \AA}$ ), operating at 40 kV and 40 mA at room temperature. Raman analysis was carried out on an inVia confocal Raman spectrophotometer (Renishaw) with an optical microscope interface (Leica) and a laser of 785 nm wavelength. Ex situ XRD and Raman of the anodes were conducted by disassembling the cells after cycling, followed by washing in 1,2-Dimethoxyethane (DME) and drying naturally in the glove box. For post-mortem morphology analysis, the SEI layer was removed from anodes by soaking the electrode in acetonitrile overnight, followed by rinsing in 0.1 mM acetic acid, deionized water, and ethanol.

**Electrochemical Measurements:** The electrochemical performance of the as-synthesized  $\text{Sb@Cu}_{15}\text{Si}_4$  NW array anodes was evaluated by assembling the CR2032 coin cells in an Ar-filled glove box (< 0.1 ppm  $\text{O}_2/\text{H}_2\text{O}$ ). The cells consisted of the  $\text{Sb@Cu}_{15}\text{Si}_4$  NW array as the working electrode, glass fiber (GF/D, Whatman) as a separator, and potassium metal (99.95%) as the counter/reference electrode. The electrolyte employed was a solution of 4 M KFSI in DME. Galvanostatic measurements were carried out using a Biologic MPG-2 in the potential range of 0.01–1.5 V (vs  $\text{K}^+/\text{K}^\ominus$ ). All current densities were calculated based on the mass of Sb. The cyclic voltammetry (CV) tests were performed at a scan rate of 0.1  $\text{mV s}^{-1}$ , and electrochemical impedance spectroscopy (EIS) measurements were computed applying an AC voltage with an amplitude of 10 mV over the frequency range: 10 kHz to 0.01 Hz. The Galvanostatic intermittent titration technique (GITT) was conducted on Biologic MPG-2 at a current density of 50  $\text{mA g}^{-1}$ , by applying Galvanostatic pulse time for 30 min, followed by rest intervals for 2 h.

## Supporting Information

Supporting Information is available from the Wiley Online Library or from the author.

## Acknowledgements

K.M.R. acknowledges Science Foundation Ireland (SFI) under the Principal Investigator Program under contract no. 16/IA/4629 and under grant no. SFI 16/M-ERA/3419 and European Union's Horizon 2020 Research and Innovation Program under grant agreement no. 814464 (Si-DRIVE project). K.M.R. further acknowledges IRCLA/2017/285 and SFI Research Centers MaREI, AMBER, and CONFIRM 12/RC/2278\_P2, 12/RC/2302\_P2, and 16/RC/3918. T.K. acknowledges support from the Sustainable Energy Authority of Ireland through the Research Development and Demonstration Funding Program (grant no. 19/RDD/548) and from Enterprise Ireland through the Innovation Partnership Program (grant no. IP 2019 0910). T.K. further acknowledges support from the SFI Research Centres MaREI (award reference no. 12/RC/2302\_P2) and AMBER (award reference no. 12/RC/2278\_P2). H.G. acknowledges SIRG under grant 18/SIRG/5484.

Open access funding provided by IREL.

## Conflict of Interest

The authors declare no conflict of interest.

## Data Availability Statement

The data that support the findings of this study are available from the corresponding author upon reasonable request.

## Keywords

copper silicide, current collectors, nanostructured antimony, nanowires, potassium ion batteries

Received: August 18, 2022

Revised: September 30, 2022

Published online:

- [1] a) J. W. Choi, D. Aurbach, *Nat. Rev. Mater.* **2016**, *1*, 16013; b) H. Kim, J. C. Kim, M. Bianchini, D.-H. Seo, J. Rodriguez-Garcia, G. Ceder, *Adv. Energy Mater.* **2018**, *8*, 1702384; c) G. Martin, L. Rentsch, M. Höck, M. Bertau, *Energy Storage Mater.* **2017**, *6*, 171; d) Z. A. Zafar, S. Imtiaz, R. Razaq, S. Ji, T. Huang, Z. Zhang, Y. Huang, J. A. Anderson, *J. Mater. Chem. A* **2017**, *5*, 5646.
- [2] a) W. L. Zhang, J. Yin, W. X. Wang, Z. Bayhan, H. N. Alshareef, *Nano Energy* **2021**, *83*, 105792; b) C. Zhang, H. Zhao, Y. Lei, *Energy Environ. Mater.* **2020**, *3*, 105; c) S.-S. Fan, H.-P. Liu, Q. Liu, C.-S. Ma, T.-F. Yi, *J. Materiomics* **2020**, *6*, 431.
- [3] I. Sultana, M. M. Rahman, Y. Chen, A. M. Glushenkov, *Adv. Funct. Mater.* **2018**, *28*, 1703857.
- [4] a) R. Rajagopalan, Y. Tang, X. Ji, C. Jia, H. Wang, *Adv. Funct. Mater.* **2020**, *30*, 1909486; b) Y.-H. Zhu, X. Yang, T. Sun, S. Wang, Y.-L. Zhao, J.-M. Yan, X.-B. Zhang, *Electrochem. Energy Rev.* **2018**, *1*, 548.
- [5] a) K. Song, C. Liu, L. Mi, S. Chou, W. Chen, C. Shen, *Small* **2019**, *15*, 1903194; b) S. Imtiaz, I. S. Amiin, Y. Xu, T. Kennedy, C. Blackman, K. M. Ryan, *Mater. Today* **2021**, *48*, 241.
- [6] a) H. Gao, X. Guo, S. Wang, F. Zhang, H. Liu, G. Wang, *EcoMat* **2020**, *2*, 12027; b) H. Tan, D. Chen, X. Rui, Y. Yu, *Adv. Funct. Mater.* **2019**, *29*, 1808745; c) W. D. McCulloch, X. Ren, M. Yu, Z. Huang, Y. Wu, *ACS Appl. Mater. Interfaces* **2015**, *7*, 26158.
- [7] V. Gabaudan, R. Berthelot, L. Stievano, L. Monconduit, *J. Phys. Chem. C* **2018**, *122*, 18266.
- [8] a) X. Yang, R. Zhang, S. Xu, D. Xu, J. Ma, Z. Zhang, S. Yang, *Chem. - Eur. J.* **2020**, *26*, 5818; b) Q. Liu, L. Fan, S. Chen, S. Su, R. Ma, X. Han, B. Lu, *Energy Technol.* **2019**, *7*, 1900634; c) X.-D. He, Z.-H. Liu, J.-Y. Liao, X. Ding, Q. Hu, L.-N. Xiao, S. Wang, C.-H. Chen, *J. Mater. Chem. A* **2019**, *7*, 9629; d) Y. Han, T. Li, Y. Li, J. Tian, Z. Yi, N. Lin, Y. Qian, *Energy Storage Mater.* **2019**, *20*, 46; e) W. Zhang, W. Miao, X. Liu, L. Li, Z. Yu, Q. Zhang, *J. Alloys Compd.* **2018**, *769*, 141.
- [9] T. Kennedy, M. Brandon, K. M. Ryan, *Adv. Mater.* **2016**, *28*, 5696.
- [10] a) L. Bazin, S. Mitra, P. L. Taberna, P. Poizot, M. Gressier, M. J. Menu, A. Barnabé, P. Simon, J. M. Tarascon, *J. Power Sources* **2009**, *188*, 578; b) X. Y. Fan, J. Han, Y. L. Ding, Y. P. Deng, D. Luo, X. Zeng, Z. Jiang, L. Gou, D. L. Li, Z. Chen, *Adv. Energy Mater.* **2019**, *9*, 1900673; c) H. Zhang, P. V. Braun, *Nano Lett.* **2012**, *12*, 2778; d) W. Wang, M. Tian, A. Abdulgatov, S. M. George, Y. C. Lee, R. Yang, *Nano Lett.* **2012**, *12*, 655.

- [11] a) H. Geaney, C. Dickinson, C. O'Dwyer, E. Mullane, A. Singh, K. M. Ryan, *Chem. Mater.* **2012**, *24*, 4319; b) I. S. Aminu, H. Geaney, S. Imtiaz, T. E. Adegoke, N. Kapuria, G. A. Collins, K. M. Ryan, *Adv. Funct. Mater.* **2020**, *30*, 2003278.
- [12] S. Hymes, K. S. Kumar, S. P. Murarka, P. J. Ding, W. Wang, W. A. Lanford, *J. Appl. Phys.* **1998**, *83*, 4507.
- [13] K. Stokes, H. Geaney, M. Sheehan, D. Borsa, K. M. Ryan, *Nano Lett.* **2019**, *19*, 8829.
- [14] C. Han, K. Han, X. Wang, C. Wang, Q. Li, J. Meng, X. Xu, Q. He, W. Luo, L. Wu, L. Mai, *Nanoscale* **2018**, *10*, 6820.
- [15] G. A. Collins, S. Kilian, H. Geaney, K. M. Ryan, *Small* **2021**, *17*, 2102333.
- [16] I. S. Amiin, N. Kapuria, T. E. Adegoke, A. Holzinger, H. Geaney, M. D. Scanlon, K. M. Ryan, *Cryst. Growth Des.* **2020**, *20*, 6677.
- [17] K. Cao, H. Liu, Y. Jia, Z. Zhang, Y. Jiang, X. Liu, K. J. Huang, L. Jiao, *Adv. Mater. Technol.* **2020**, *5*, 2000199.
- [18] a) Q. Liu, L. Fan, R. Ma, S. Chen, X. Yu, H. Yang, Y. Xie, X. Han, B. Lu, *Chem. Commun.* **2018**, *54*, 11773; b) Y. An, Y. Tian, L. Ci, S. Xiong, J. Feng, Y. Qian, *ACS nano* **2018**, *12*, 12932; c) C. Wei, D. Gong, D. Xie, Y. Tang, *ACS Energy Lett.* **2021**, *6*, 4336.
- [19] a) Y. Tian, Y. An, S. Xiong, J. Feng, Y. Qian, *J. Mater. Chem. A* **2019**, *7*, 9716; b) Z. Yi, N. Lin, W. Zhang, W. Wang, Y. Zhu, Y. Qian, *Nanoscale* **2018**, *10*, 13236; c) X. Ge, S. Liu, M. Qiao, Y. Du, Y. Li, J. Bao, X. Zhou, *Angew. Chem., Int. Ed. Engl.* **2019**, *58*, 14578.
- [20] a) S. Imtiaz, I. S. Amiin, D. Storan, N. Kapuria, H. Geaney, T. Kennedy, K. M. Ryan, *Adv. Mater.* **2021**, *33*, 2105917; b) Y. Shi, L. Wang, D. Zhou, T. Wu, Z. Xiao, *Appl. Surf. Sci.* **2022**, *583*, 152509; c) B. Chen, L. Yang, X. Bai, Q. Wu, M. Liang, Y. Wang, N. Zhao, C. Shi, B. Zhou, C. He, *Small* **2021**, *17*, e2006824.
- [21] Z. Huang, Z. Chen, S. Ding, C. Chen, M. Zhang, *Solid State Ion* **2018**, *324*, 267.
- [22] Z. Yan, Z. Huang, Y. Yao, X. Yang, H. Li, C. Xu, Y. Kuang, H. Zhou, *J. Alloys Compd.* **2021**, 858.
- [23] W. Luo, F. Li, W. Zhang, K. Han, J.-J. Gaumet, H.-E. Schaefer, L. Mai, *Nano Res.* **2019**, *12*, 1025.
- [24] a) N. Drewett, J. Gómez-Cámer, B. Acebedo, M. Galceran, T. Rojo, *Batteries* **2017**, *3*, 20; b) Y. Hu, Q. Qiu, X. Zhu, T. Lai, *Appl. Surf. Sci.* **2020**, *505*, 144337.
- [25] a) T. Kennedy, E. Mullane, H. Geaney, M. Osiak, C. O'Dwyer, K. M. Ryan, *Nano Lett.* **2014**, *14*, 716; b) X. H. Liu, S. Huang, S. T. Picraux, J. Li, T. Zhu, J. Y. Huang, *Nano Lett.* **2011**, *11*, 3991; c) Q. Chen, K. Sieradzki, *Nat. Mater.* **2013**, *12*, 1102.
- [26] a) S. Kilian, K. McCarthy, K. Stokes, T. E. Adegoke, M. Conroy, I. S. Amiin, H. Geaney, T. Kennedy, K. M. Ryan, *Small* **2021**, *17*, 2005443; b) K. Stokes, G. Flynn, H. Geaney, G. Bree, K. M. Ryan, *Nano Lett.* **2018**, *18*, 5569.
- [27] T. Kennedy, M. Bezuidenhout, K. Palaniappan, K. Stokes, M. Brandon, K. M. Ryan, *ACS Nano* **2015**, *9*, 7456.
- [28] a) X. H. Rui, N. Yesibolati, S. R. Li, C. C. Yuan, C. H. Chen, *Solid State Ion* **2011**, *187*, 58; b) X. Huang, J. Zhao, W. Zhu, M. Hou, T. Zhou, L. Bu, L. Gao, W. Zhang, *J. Energy Chem.* **2021**, *63*, 376.
- [29] a) Y. Wu, J. Zheng, Y. Tong, X. Liu, Y. Sun, L. Niu, H. Li, *ACS Appl. Mater. Interfaces* **2021**, *13*, 51066; b) H. Gao, Y. Wang, Z. Guo, B. Yu, G. Cheng, W. Yang, Z. Zhang, *J. Energy Chem.* **2022**, *75*, 154.
- [30] a) Y. Zhao, X. Ren, Z. Xing, D. Zhu, W. Tian, C. Guan, Y. Yang, W. Qin, J. Wang, L. Zhang, Y. Huang, W. Wen, X. Li, R. Tai, *Small* **2020**, *16*, e1905789; b) M. K. Jangid, A. S. Lakhnot, A. Vemulapally, F. J. Sonia, S. Sinha, R. O. Dusane, A. Mukhopadhyay, *J. Mater. Chem. A* **2018**, *6*, 3422; c) R. Lin, S. Zhang, Z. Du, H. Fang, Y. Ren, X. Wu, *RSC Adv.* **2015**, *5*, 87090.
- [31] G.-T. Kim, T. Kennedy, M. Brandon, H. Geaney, K. M. Ryan, S. Passerini, G. B. Appetecchi, *ACS Nano* **2017**, *11*, 5933.